Dark Count Rate and Time Resolution Measurment of SiPMs

Author: Lai Gui
Supervisor: Esteban Currás Rivera

Laboratoire de Physique des Hautes Énergies
École Polytechnique Fédérale de Lausanne

November 13, 2025

Travail de Spécialisation pour Master en physique (TSM)
PHYS-597

Overview

This report is divided into two main sections:

1. **Time Resolution Measurement under Varying Laser Intensity Conditions**
2. **Dark Count Rate Measurement of Irradiated SiPMs down to 100 K**

Both studies focus on evaluating key performance aspects of silicon photomultipliers (SiPMs), yet they differ significantly in their objectives and experimental methodologies. The first part investigates the timing characteristics of SiPMs by examining their Single Photon Time Resolution (SPTR) under controlled laser illumination, while the second part explores the dark count rate behaviour of irradiated SiPMs at cryogenic temperatures. Although these experiments share a common theme of SiPM characterisation, they are presented as distinct sections to ensure clarity and coherence in discussing their respective setups, analyses, and results.

Contents

Part I
Time Resolution Measurement Under Varying Laser Intensity Conditions

Abstract

This experiment investigates the time resolution of single-cell FBK silicon photomultipliers (SiPMs), focusing primarily on devices with a 42 µm cell size featuring a metal layer, under varying incident laser intensities. Since the laser emission follows a temporal probability distribution, the SiPM is expected to trigger preferentially on the earliest arriving photons when the illumination is sufficiently strong. This effect enables a more accurate measurement of the Single Photon Time Resolution (SPTR) by minimising the contribution from laser pulse statistics. The results show that the SPTR improves (i.e., FWHM decreases) with increasing light intensity at low illumination levels, reaching a saturation point at approximately 0.7 µA. Beyond this point, occasional early waveforms emerge, leading to a degradation in timing precision. The underlying mechanism for this behaviour, as well as an increase in the signal amplitude at higher laser intensities remain to be clarified.

I.1 Introduction

I.1.1 LHCb

LHCb (Large Hadron Collider beauty experiment) is one of the four main experiments at the Large Hadron Collider (LHC) at CERN, as shown in Fig. 1. It records data from proton–proton collision events using a series of high-precision detectors to reconstruct the underlying physical processes occurring at the interaction point. By probing matter and fundamental forces at extremely small distance scales and high energies (conditions similar to those just after the Big Bang), LHCb contributes to our understanding of the structure and evolution of the universe.

In LHCb, Silicon Photomultipliers (SiPMs) are coupled to scintillating fibres (SciFi) within the tracking system to provide precise position measurements of charged particles, as illustrated in Fig. 2. When a charged particle passes through the SciFi detector, it excites the scintillating fibres, which then emit photons that are detected by the SiPMs. This process allows the reconstruction of particle trajectories with high spatial and temporal accuracy.

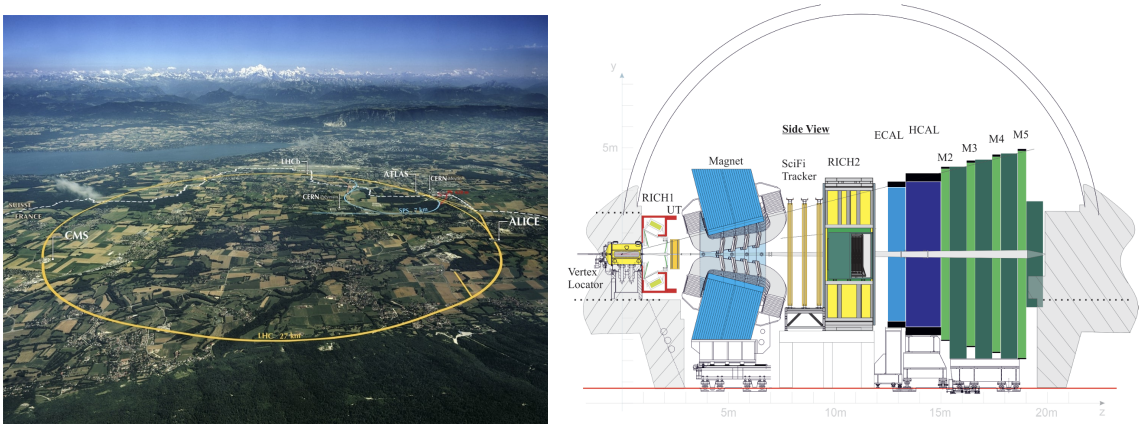

Figure 1: Left: Aerial view of the LHC and its four major experiments [1]. Right: Schematic layout of the LHCb detector [2].

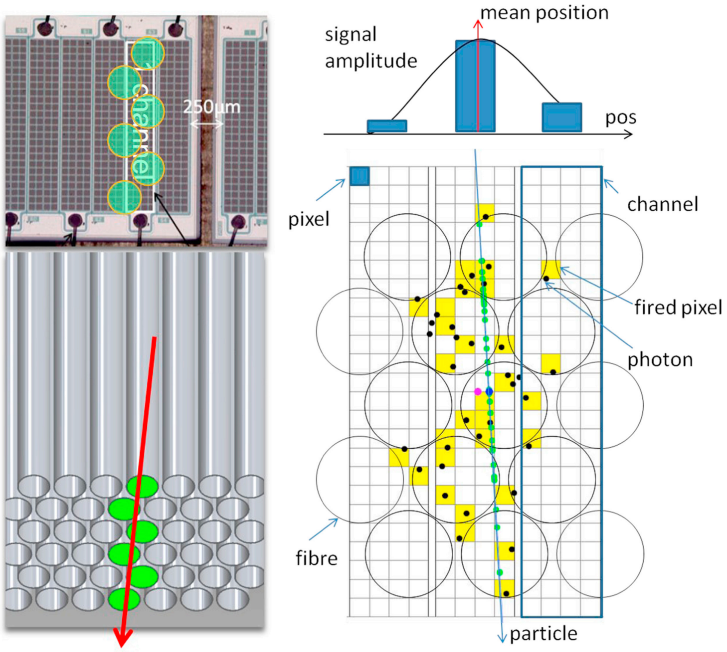

Figure 2: Illustration of particle detection using scintillating fibres coupled to SiPMs [3]. Scintillating photons emitted from the fibres are received by the SiPMs to allow particle trajectory reconstruction.

Since many particles pass through the detector simultaneously, the timing resolution of the SiPMs is crucial for distinguishing signals from different events and ensuring accurate particle identification.

I.1.2 Silicon Photomultiplier (SiPM)

A Silicon Photomultiplier (SiPM) is a solid-state photodetector consisting of an array of microcells, each being a Single-Photon Avalanche Diode (SPAD), as illustrated in Fig. 3. Each SPAD operates under a bias voltage exceeding its breakdown voltage, a regime known as Geiger mode (Fig. 4).

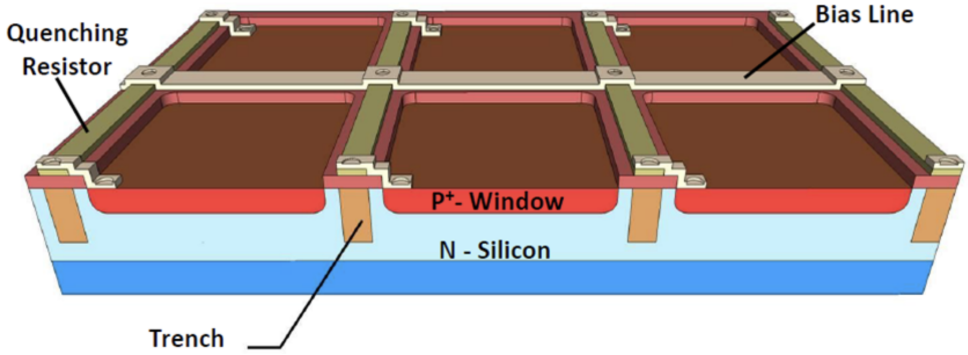

Figure 3: Schematic structure of a SiPM composed of an array of SPAD (Single-Photon Avalanche Diode) microcells [4]. Each microcell contains a quenching resistor, a bias line, and a p^+ window on an n-type silicon substrate. Trenches between microcells provide optical isolation to suppress crosstalk.

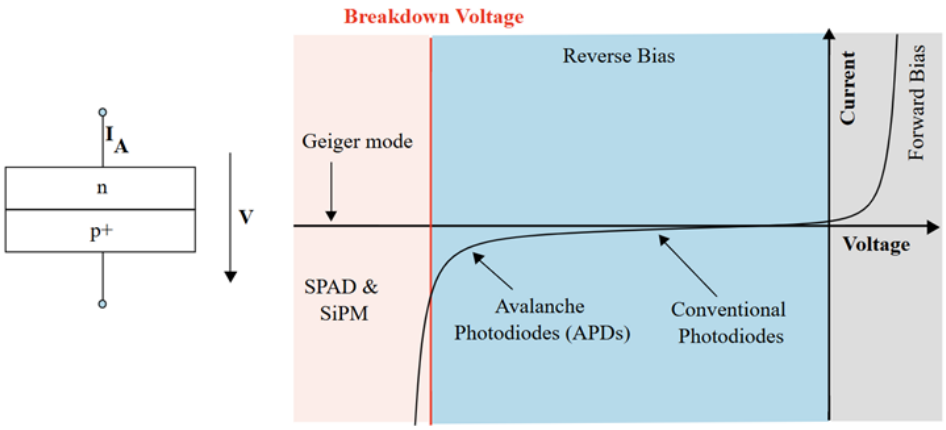

Figure 4: Current–voltage characteristic of a SPAD microcell [5]. In Geiger mode, the SPAD is reverse-biased above its breakdown voltage, enabling avalanche multiplication triggered by the absorption of a single photon.

When biased below the breakdown voltage (i.e., in linear avalanche photodiode (APD) mode), impact ionisation is primarily driven by electrons, which are more mobile than

holes, as they drift toward the cathode. However, in Geiger mode, both electrons and holes gain sufficient energy to initiate secondary ionisations. This mutual ionisation results in a self-sustaining avalanche current once triggered by a single photon.

Because the avalanche process cannot cease spontaneously, each SPAD microcell incorporates a quenching resistor. The resistor momentarily limits the current and drops the bias voltage below breakdown, thereby quenching the avalanche and allowing the microcell to recover for subsequent detections.

When multiple SPAD microcells are illuminated, avalanches occur independently across them. The SiPM output is the analog sum of the currents from all fired microcells, making the total signal approximately proportional to the number of detected photons. At high illumination levels, however, a large fraction of the microcells may fire simultaneously, causing saturation, which is a nonlinear response where the output no longer accurately reflects the incident photon intensity.

I.1.3 Single Photon Time Resolution (SPTR)

To evaluate the performance of SiPMs in determining the arrival time of incident particles, it is essential to measure their Single Photon Time Resolution (SPTR). Under single-photon detection conditions, an SiPM exhibits its poorest timing resolution; therefore, the SPTR defines the lower performance limit of the device.

The SPTR quantifies the temporal spread of the SiPM's response to single-photon events. It reflects the device's capability to reconstruct the photon time of arrival, which is critical for precise track and vertex reconstruction in high-energy physics experiments such as LHCb.

Several physical and instrumental factors contribute to the overall SPTR of an SiPM. The five dominant sources of timing uncertainty are summarised below:

1. Intrinsic error: Non-uniformities in the electric field within each SPAD microcell cause variations in carrier drift velocity depending on where the photon is absorbed. The field is strongest near the centre of the microcell, leading to faster avalanche initiation there. This spatial dependence introduces a spread in detection times. The effect can be mitigated using microlens arrays to focus photons toward the centre of each microcell. Additional variations arising from microscopic differences in SPAD structure during fabrication also contribute to the intrinsic spread.

2. Transit time skew: The signal readout path is not equidistant from all microcells. Consequently, avalanches initiated in SPADs closer to the output node reach the readout circuit slightly earlier than those further away, introducing a systematic spatial bias in timing. This effect can be characterised experimentally by masking different SiPM regions and comparing their relative timing responses.

3. Trigger time error: The laser source provides a trigger signal marking the photon emission time. The SiPM signal is measured relative to this trigger. However, the trigger itself has an timing uncertainty, though not independently measured in this study.

4. Laser uncertainty: Beyond trigger uncertainty, the laser pulse exhibits a temporal spread with respect to its nominal emission time. For the laser model and power level used in this experiment, this spread is approximately 56 ps, contributing directly to the measured SPTR.

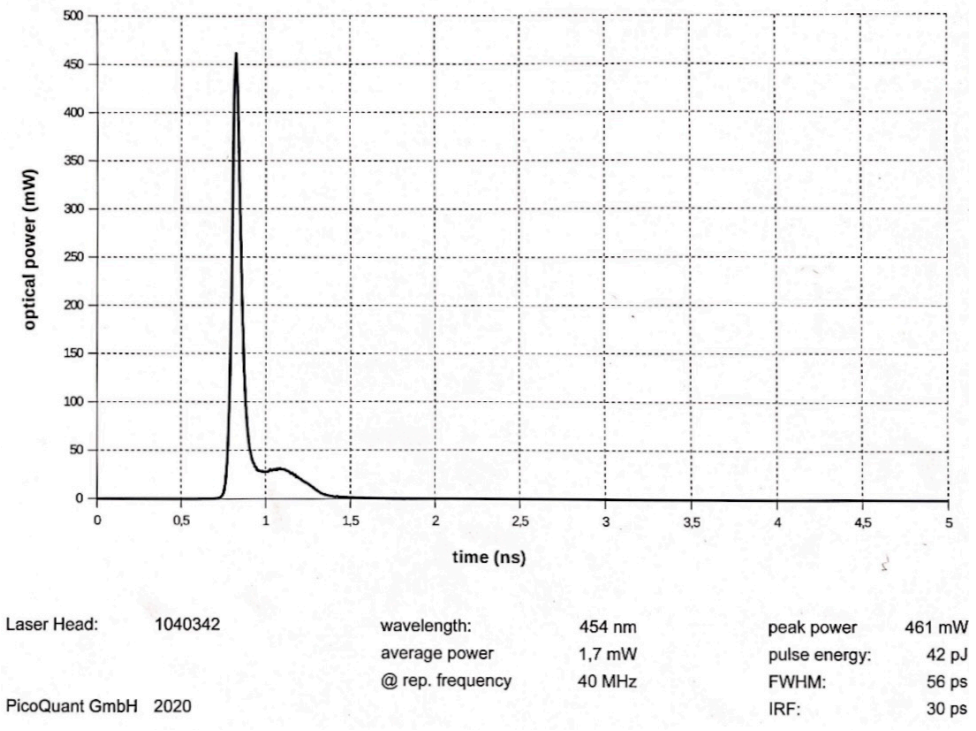

Figure 5: Laser optical power as a function of time [6]. The width of this power distribution contributes directly to the overall SPTR.

5. Electronic jitter: Electronic noise in the signal processing chain introduces timing uncertainty, commonly referred to as jitter, as illustrated in Fig. 6. This effect becomes more pronounced for signals with smaller amplitudes, where the timing determination depends more sensitively on baseline fluctuations. The jitter contribution can be estimated from the ratio between the baseline noise standard deviation and the slope of the signal's leading edge.

The total SPTR can be expressed as the quadratic sum of the individual contributions:

$$\mathrm{FWHM}^2_{\mathrm{Total}} = \mathrm{FWHM}^2_{\mathrm{Intrinsic}} + \mathrm{FWHM}^2_{\mathrm{Transit}} + \mathrm{FWHM}^2_{\mathrm{Trigger}} + \mathrm{FWHM}^2_{\mathrm{Laser}} + \mathrm{FWHM}^2_{\mathrm{Jitter}} \tag{1}$$

In this study, single-cell SiPMs were used, thereby eliminating the contribution from transit time skew. The jitter contribution was evaluated from baseline fluctuations and signal amplitude. The trigger uncertainty, specified as < 20 ps by the manufacturer, could

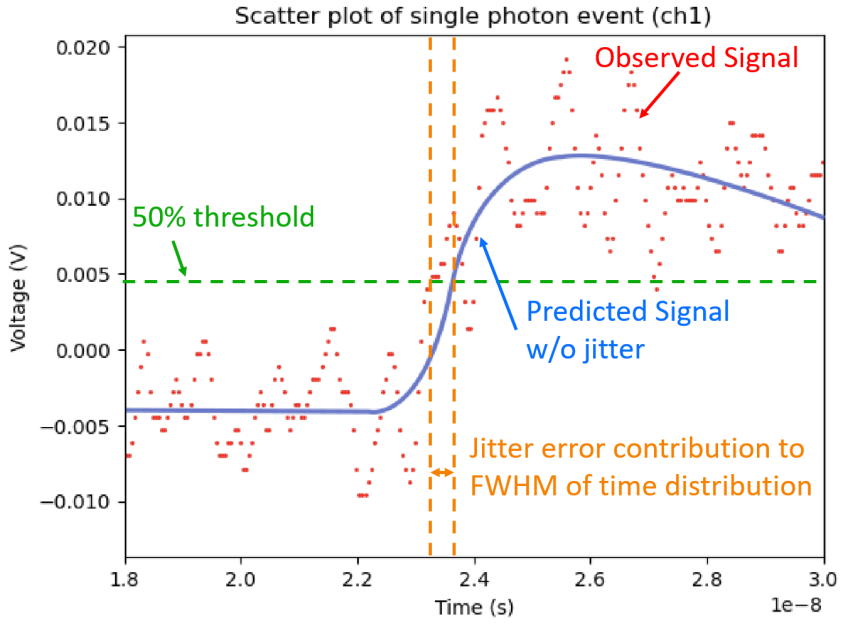

Figure 6: Illustration of jitter-induced timing uncertainty. Random fluctuations in the waveform cause variations in the threshold crossing point, resulting in a spread in the measured arrival time.

not be independently verified in our experimental setup. Furthermore, by increasing the illumination intensity, the SiPM always triggers on the photons emitted at the leading edge of the laser optical power distribution (Fig. 5). This effectively suppresses the influence of the laser time spread, enabling a purer measurement of the SiPM's intrinsic SPTR.

Such an approach facilitates a more accurate characterisation of SiPM timing performance, which is essential for optimisation and preparation for future LHCb detector upgrades.

I.2 Methodology

I.2.1 Experimental Setup

A photograph of the experimental setup is shown in Fig. 7. The system consists of a pulsed laser source, a bias power supply, an oscilloscope, and a computer for data acquisition and analysis. The SiPM under test is enclosed in a shielded (Faraday) box to suppress electromagnetic interference and block ambient light. Inside the box, the SiPM is mounted on a readout board, and its output signal is amplified by a 40 dB amplifier before being digitised by the oscilloscope. The recorded waveforms are then transmitted

to the computer for further processing.

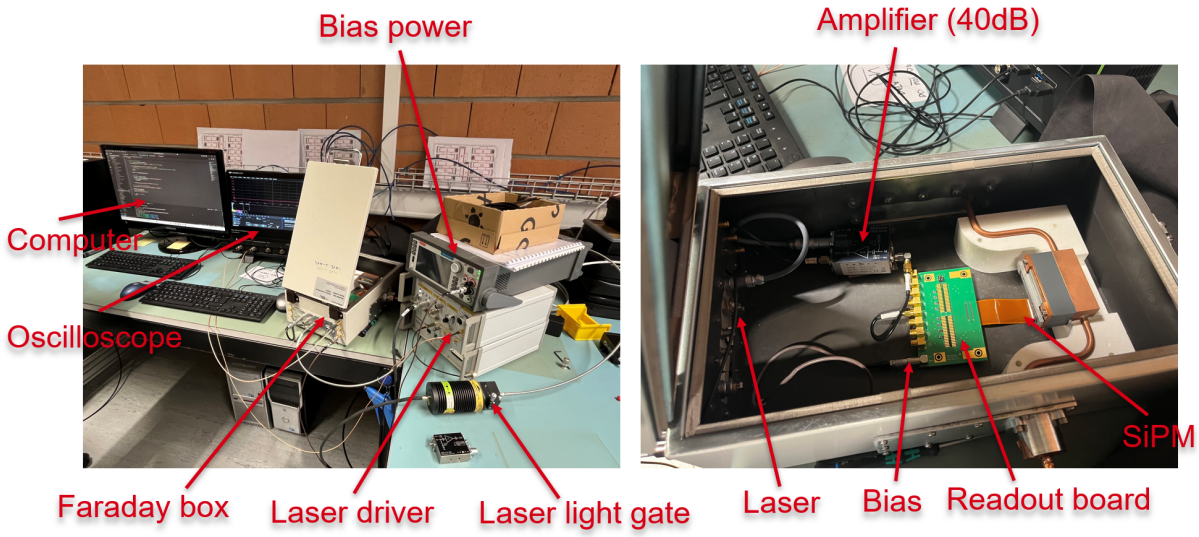

Figure 7: **Left:** Overall experimental setup consisting of a computer, oscilloscope, Faraday box, laser driver with laser head, and bias power supply. **Right:** Inside the Faraday box, the SiPM under test is connected to a readout board and a 40 dB amplifier.

The device tested is a 42 µm single-cell SiPM (FBK Wafer 1) with metal layer, shown in Fig. 8. This configuration ensures that transit time skew, as described in Sec. I.1.3, is eliminated from the measurement. The single-pixel nature of the SiPM also excludes the potential contributions from other cells, ensuring single-photon detection events even at high laser intensities.

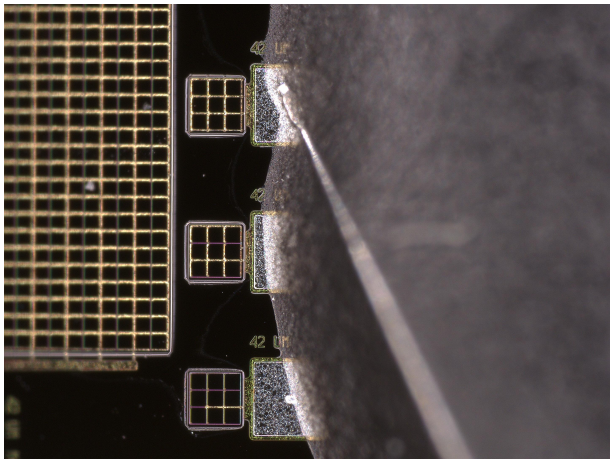

Figure 8: 42 µm single-cell SiPM used for SPTR measurements. Only the cell with full metal layer (on the top) is investigated.

I.2.2 Laser Intensity Adjustment

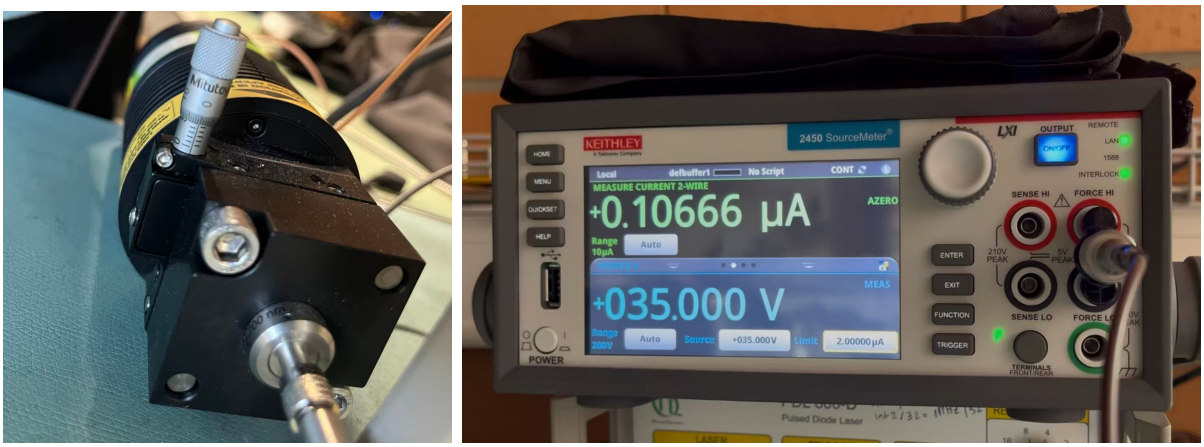

Figure 9: **Left**: Laser head with an adjustable aperture knob to tune output intensity. **Right**: Bias power supply used to set the SiPM bias voltage and monitor the operating current.

The SiPM is placed close to the laser output and aligned as accurately as possible. The laser head includes an adjustable aperture (Fig. 9), which controls the emitted optical power. By increasing the aperture size, the optical intensity incident on the SiPM increases. However, the laser aperture control is not linearly correlated with the optical intensity. Therefore, instead of relying on the aperture knob position, the SiPM current at a fixed bias of 35 V is used as a proxy for the relative laser intensity. This approach provides a reasonable estimate before the SiPM reaches saturation, which is when not every laser pulse corresponds to a distinct photon detection event. Beyond saturation, the measured current continues to increase even though the photon detection probability per pulse has reached its limit.

A more accurate calibration could be achieved in future measurements by using a spectrometer or a calibrated photodiode to quantify the laser intensity.

I.2.3 Data Acquisition

The oscilloscope is triggered on the laser synchronisation output, while the SiPM signal waveform is recorded on the second channel (Fig. 10). Prior to data acquisition, the breakdown voltage of each SiPM channel is determined by linearly extrapolating the signal amplitude as a function of bias voltage around the nominal breakdown point.

Figure 10: Oscilloscope used for SiPM waveform acquisition. The laser trigger serves as the time reference.

For all measurements, the SiPM overvoltage (OV) is scanned from 2.0 V to 9.0 V in 0.5 V increments. At each voltage setting, 50,000 waveforms are collected for statistical analysis. The breakdown voltage is extracted by plotting the signal amplitude as a function of bias voltage and performing a linear extrapolation to zero amplitude, which defines the onset of avalanche multiplication.

I.3 Analysis

I.3.1 Single-Photon Event Extraction

A time window is defined around the expected signal peak to isolate single-photon events. Two types of filters are applied: (1) a **baseline filter**, applied before the time window to remove events superimposed on dark count residuals, and (2) a **time-window filter**,

applied within the window to isolate single-photon pulses from baseline-only events.

When the laser intensity is low, filtering within the time window is more critical; at higher intensities, baseline filtering becomes more prominent.

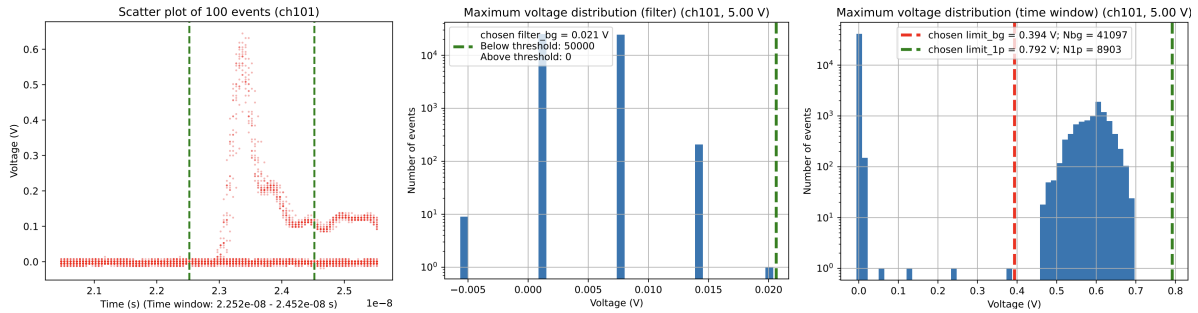

Figure 11: **Left**: waveforms at 0.1 µA laser intensity; **Middle**: baseline filtering before the time window; **Right**: signal filtering within the time window. When the laser intensity is low, signal filtering is more important.

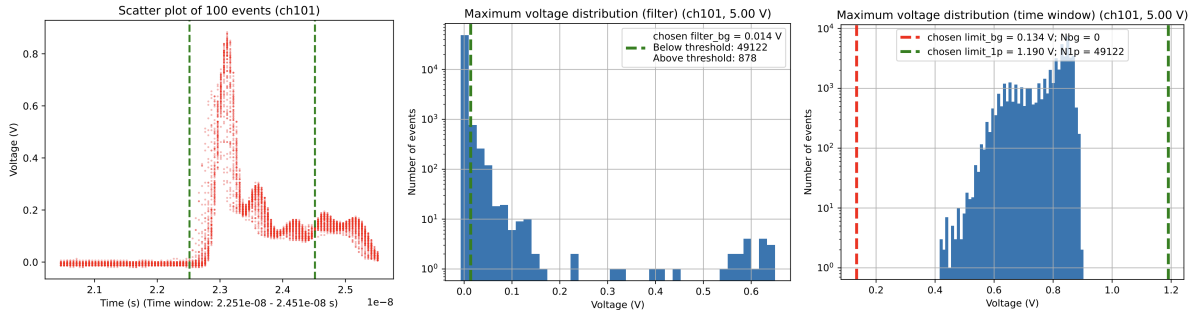

Figure 12: **Left**: waveforms at 1.1 µA; **Middle**: baseline filtering before the time window; **Right**: signal filtering within the time window. When the laser intensity is high, baseline filtering is more important.

I.3.2 FWHM Extraction

After filtering, a threshold is applied to extract the timing distribution. Each distribution is then fitted with a Gaussian function to obtain the FWHM as a representation of the SPTR. As shown in Fig. 13, while not always a perfect model, it provides a consistent basis for FWHM estimation across datasets.

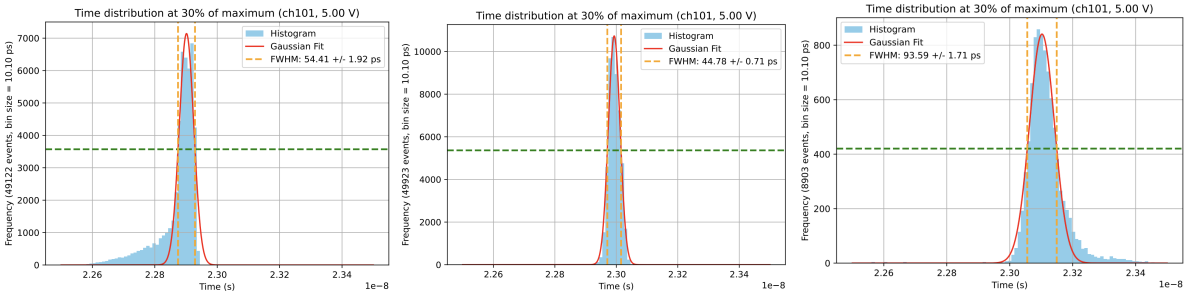

Figure 13: Gaussian fitting of the time distribution at 30% threshold for 1.1 µA (left), 0.7 µA (middle), and 0.1 µA (right).

Differences in the time distributions at various intensities arise from the distinct waveform characteristics, as shown in Fig. 14.

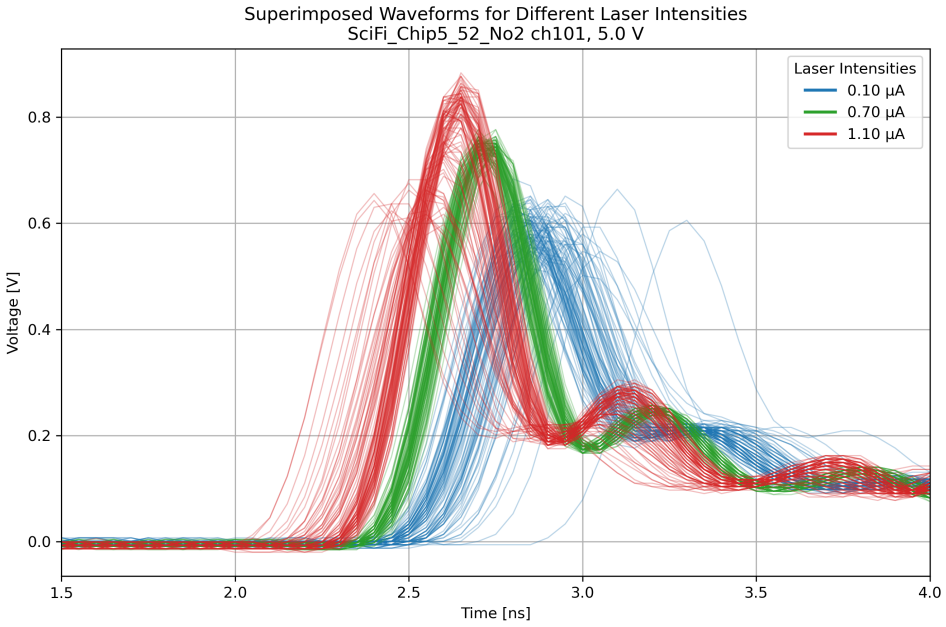

Figure 14: Comparison of 100 representative filtered single-photon waveforms at 0.1 µA, 0.7 µA, and 1.1 µA.

At low intensity, delayed photons are visible, consistent with the broader optical pulse width of the laser. Increasing the intensity to around 0.7 µA enhances the signal amplitude and yields the best time resolution. Beyond this, early-arriving photons begin to appear, suggesting potential saturation effects.

For each overvoltage, the FWHM is determined by scanning different thresholds and averaging the three lowest values, as shown in Fig. 15.

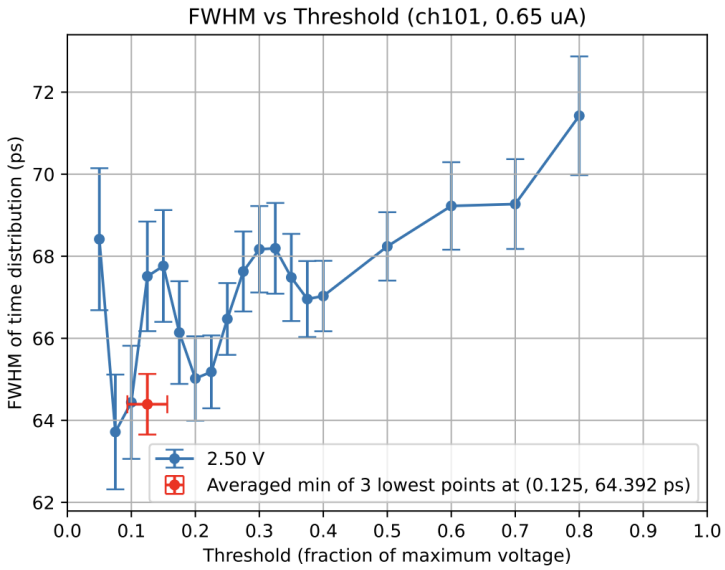

Figure 15: Threshold scan at 0.65 µA and 2.5 V overvoltage. The average of the three minima is used as the representative FWHM.

This procedure is repeated for all laser intensities and overvoltages to produce the results in Fig. 16. The optimal FWHM occurs around 0.7 µA, corresponding to an intermediate photon flux.

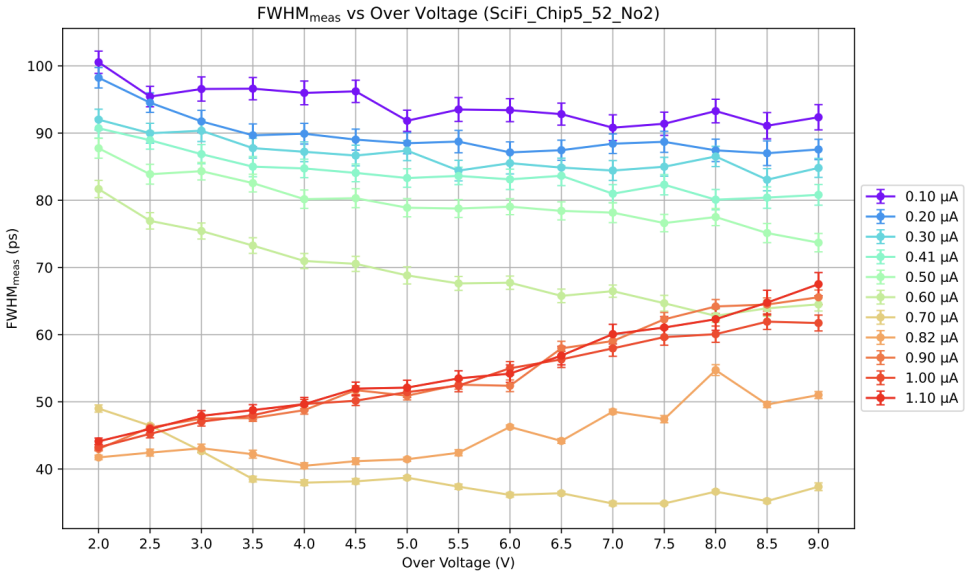

Figure 16: Measured FWHM versus overvoltage for different laser intensities. The total width includes intrinsic detector timing spread, electronic jitter, and trigger timing error.

I.3.3 Jitter Error Analysis

The contribution of electronic jitter to the total FWHM is estimated using:

$$\mathrm{FWHM}_{\mathrm{jitter}} = 2.3458 \times \frac{\sigma_{\mathrm{background}}}{\text{average gradient}}, \tag{2}$$

where the factor 2.3458 converts the Gaussian standard deviation to FWHM. Here, $\sigma_{\mathrm{background}}$ represents the standard deviation of the baseline noise, and the average gradient refers to the signal's leading-edge slope at where the minimal FWHM occurs. These two quantities can be measured and plotted as shown in Fig. 17 and Fig. 18 respectively.

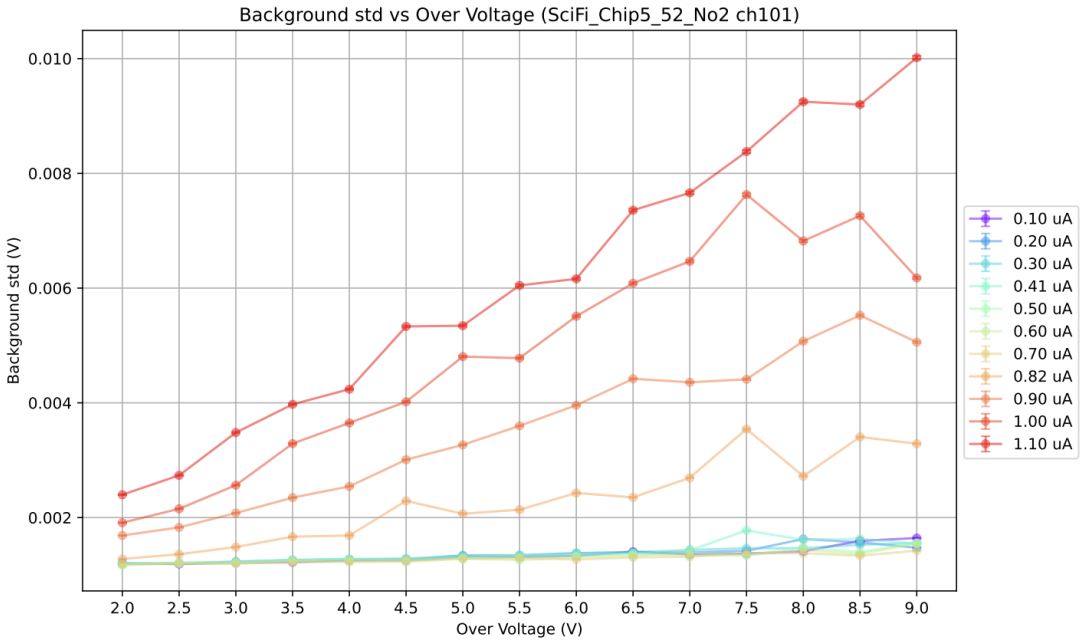

Figure 17: Baseline noise standard deviation as a function of overvoltage. Higher overvoltage introduces a higher baseline fluctuation. This is especially prominent for higher laser intensities.

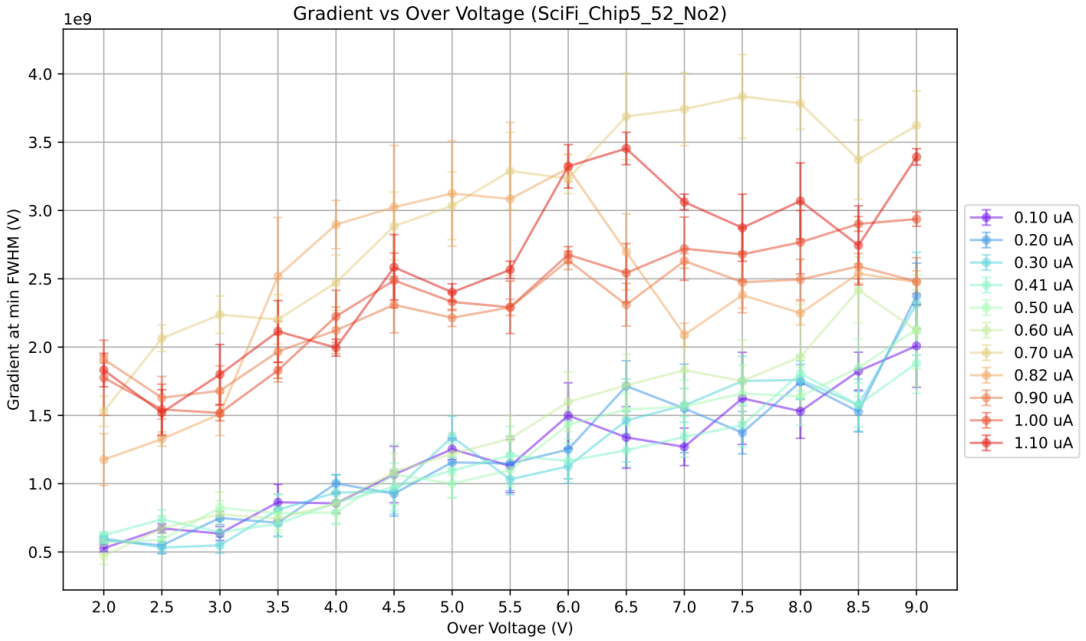

Figure 18: Average signal gradient at the threshold corresponding to minimal FWHM (as in Fig. 15). Generally higher laser intensities causes a higher signal gradient, probably due to the increased amplitude.

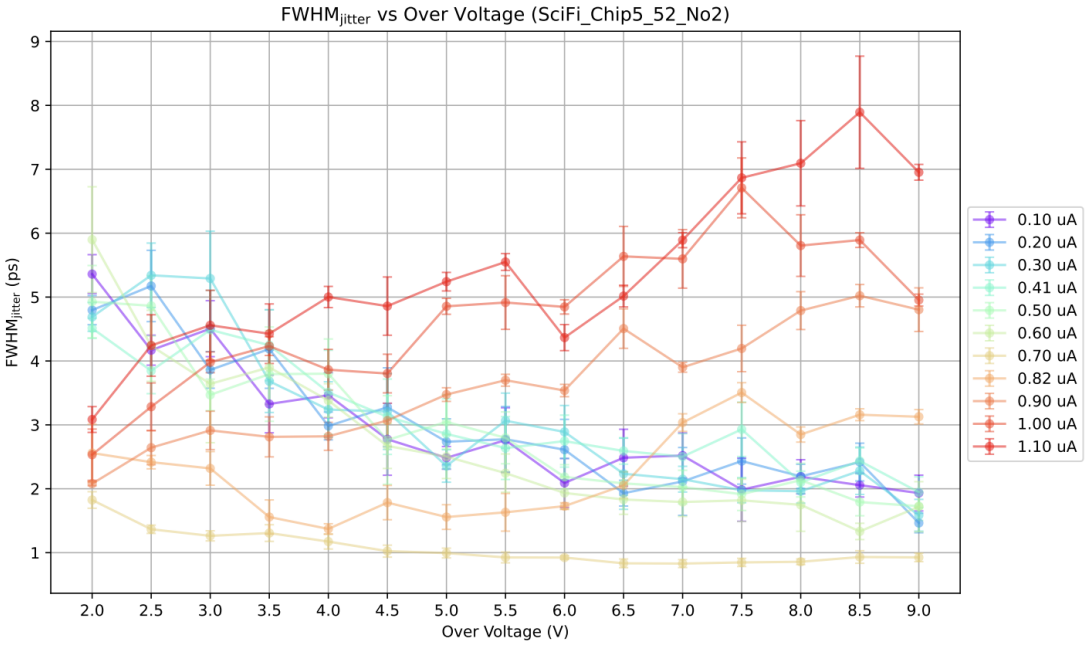

Figure 19: Estimated FWHM contribution from jitter, computed using Eqn. 2.

The jitter contribution can therefore be calculated using Eqn. 2, and is shown in Fig. 19. Subtracting this component from the measured width yields the intrinsic timing resolution of the SiPM:

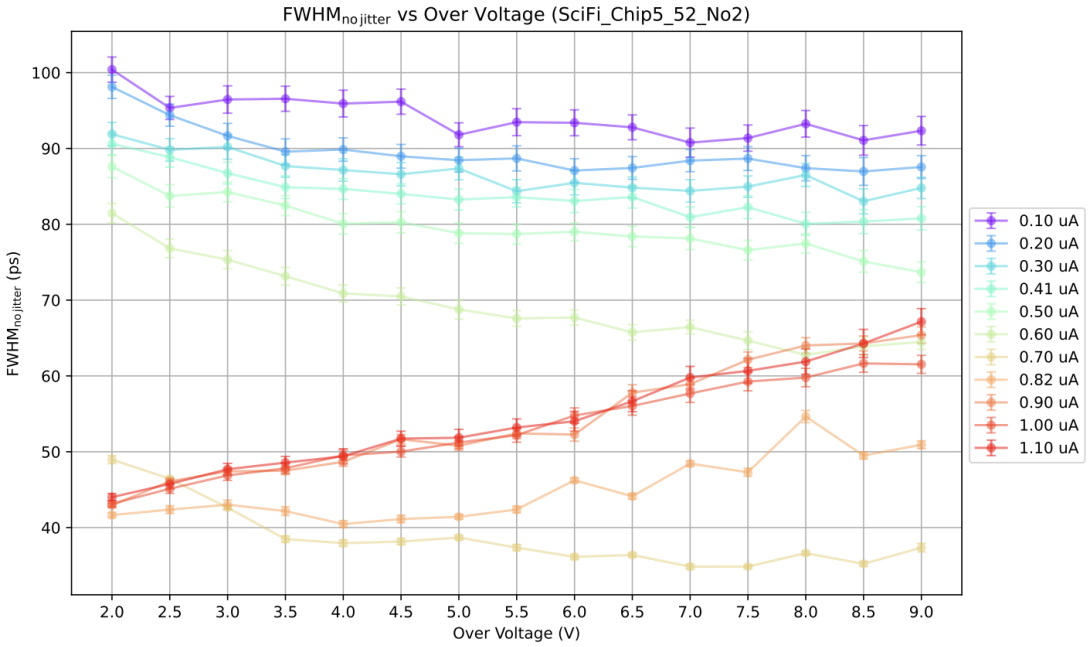

Figure 20: FWHM after correction for electronic jitter contribution.

The best SPTR occurs with 0.70 µA laser intensity, and has a value of about 35 ps. This number is significantly lower than about 90 ps at the laser intensity of 0.10 µA. This reduce can be concluded as a result of exclusion of the laser uncertainty. By comparing the two extrema of the FWHM, the uncertainty of the laser can be obtained to be approximately 80 ps, which is larger than the 56 ps uncertainty as claimed by the manufacturer.

I.3.4 Amplitude Analysis

To compare average pulse shapes at different intensities, all waveforms are aligned at their 50% threshold crossing points. The averaged pulse shapes at each laser intensity can hence be plotted in Fig. 21.

One possibility of this effect is that at low intensities, some photons may impinge on regions with lower local electric fields, resulting in smaller pulse amplitudes. As the intensity increases, more photons reach the central, high-field regions, producing higher and more uniform amplitudes. The observed saturation at high intensity suggests that the SiPM is approaching its full charge multiplication capacity.

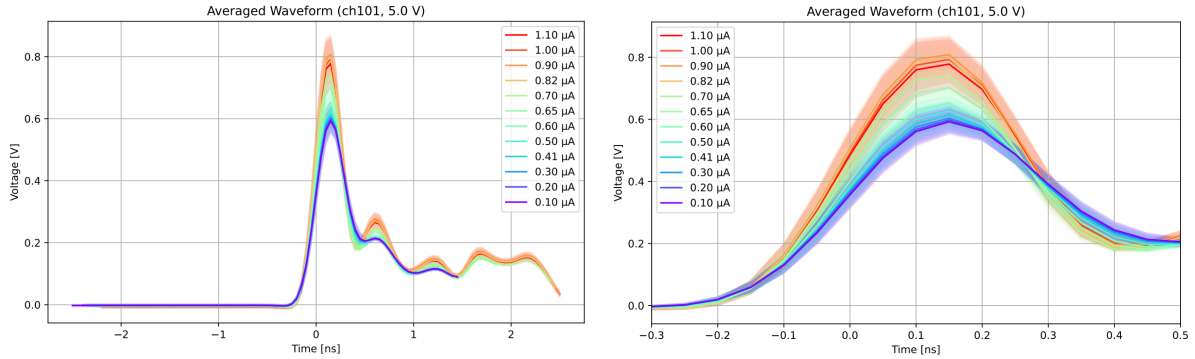

Figure 21: **Left**: averaged waveforms aligned at 50% threshold crossing. The integrated area increases with laser intensity, indicating higher charge collection (gain). **Right**: zoomed-in view of the peak region, showing amplitude saturation beyond 0.82 µA.

I.4 Discussion

The best timing resolution achieved in this measurement is a FWHM of 35 ps, corresponding to a temporal spread (standard deviation) of approximately 15 ps. This translates to a spatial resolution of about 5 mm for particles travelling at the speed of light, demonstrating the excellent timing capability of the SiPM under test. Comparing the results obtained at different illumination levels, we observe that the FWHM improves from about 90 ps at 0.1 µA to 35 ps at 0.7 µA. Assuming that the SiPM intrinsic error and trigger error contributions remain constant, this difference allows us to estimate the laser uncertainty introduced by the optical power distribution of the laser itself to be around 80 ps. This value is notably higher than the 56 ps specified by the manufacturer, suggesting that a potential re-calibration of the laser is needed, or there are other factors, such as the fibre total internal reflection, that are also contributing to the SiPM time resolution measurement.

In addition to the timing performance, the amplitude of the detected signals shows a strong dependence on the incident light intensity. At low currents, the signal amplitude increases proportionally with illumination; however, beyond approximately 0.8 µA, the response begins to saturate. This behaviour indicates that the SiPM reaches a regime where multiple photons may simultaneously trigger the same microcell. The apparent increase in gain at higher intensities might therefore not correspond to a true gain enhancement, but rather to the summation of overlapping photon detection events. Further investigation is needed to clarify this nonlinear behaviour.

The current method of laser intensity measurement using the SiPM current at a fixed bias to infer the relative laser intensity provides a rough estimate but introduces significant uncertainties, particularly near and beyond saturation. Employing a calibrated photodiode or spectrometer to directly measure the laser output would yield a more accurate

description of the optical power and its variation with the aperture setting. Additionally, repeating the experiment with a different or newly calibrated laser head would help isolate whether the observed broadening of the timing distribution originates from the laser itself or from the measurement setup.

Finally, another way to reduce the laser uncertainty contribution is using a laser with a shorter pulse width or faster trigger synchronisation. The optical path differences within the fibre and the alignment between the laser and SiPM could also introduce additional timing dispersion, and should therefore be characterised in future work. Overall, while the achieved resolution demonstrates the potential of single-pixel SiPMs for precise timing applications, a more controlled optical setup and laser calibration are essential to fully exploit their intrinsic performance.

Part II
Dark Count Rate Measurement of Irradiated SiPMs down to 100K

Abstract

This study investigates the dark count rate (DCR) of neutron-irradiated Silicon Photomultipliers (SiPMs) operated at a cryogenic temperature of 100 K. The original aim of the study was to test the behaviour of SiPMs exposed to neutron fluences of $1 \times 10^{13}\,\mathrm{n_{eq}/cm^2}$, $3 \times 10^{12}\,\mathrm{n_{eq}/cm^2}$, $1 \times 10^{12}\,\mathrm{n_{eq}/cm^2}$ and $3 \times 10^{11}\,\mathrm{n_{eq}/cm^2}$, however owing to the packaging issues, some of the SiPM cells are detached from the detectors during cooling down, leaving the SiPM with $1 \times 10^{13}\,\mathrm{n_{eq}/cm^2}$ to be the only available option for this study. Meanwhile the remaining ones have been fixed and will be investigated in the future work.

The DCR was measured at different overvoltages, exhibiting the expected increase with bias. Time-separation and amplitude analyses were employed to suppress electronic noise and isolate valid avalanche events, from which the DCR was extracted through Poisson fitting. Deviations from ideal Poisson statistics were observed and attributed to correlated noise sources such as afterpulsing and recovery-time effects. These effects show a clear dependence on the DCR and are likely influenced by temperature and accumulated radiation damage. Further studies across varying fluence levels and operating conditions are proposed to better quantify these dependencies.

II.1 Introduction

II.1.1 Dark Count Rate (DCR)

Thermal noise is generated inside Silicon Photomultipliers (SiPMs) due to inhomogeneities within the silicon lattice structure, which originate from manufacturing imperfections and potential radiation-induced defects. The resulting thermally generated carriers can trigger avalanches, giving rise to the Dark Count Rate (DCR).

Several factors contributing to the DCR include:

1. **Temperature:** Higher temperature increases the likelihood of thermal activation of carriers within the depletion region. The DCR exhibits an exponential dependence on temperature:

$$\mathrm{DCR} \propto \exp\left(-\frac{E_a}{kT}\right), \tag{3}$$

where E_a is the activation energy for carrier generation, k is the Boltzmann constant, and T is the absolute temperature in *Kelvin (K)*.

2. **Overvoltage:** Increasing the overvoltage enhances the electric field within each microcell, thereby increasing the probability that a thermally generated carrier will trigger an avalanche.

3. **Pixel Size:** Larger pixels have a greater active volume for thermal carrier generation, leading to a proportionally higher DCR.

4. **Radiation Damage:** Exposure to ionising radiation, particularly neutron or proton fluence, introduces defects in the silicon lattice that act as trap states. These traps serve as trap-assisted tunneling (TAT) centers, enhancing both dark count and afterpulse generation. This effect becomes especially significant in high-radiation environments at cryogenic temperature of less than 150 K, such as collider experiments (e.g., LHCb).

Under standard operating conditions, the dark count generation in an SiPM follows a Poisson distribution:

$$P(n;\lambda) = \frac{(\lambda t)^n e^{-\lambda t}}{n!} \quad \Rightarrow \quad P(n=0;\lambda) = e^{-\lambda t}, \tag{4}$$

where λ represents the rate of dark counts.

However, in the presence of severe radiation damage or when the pixel recovery time becomes comparable to the average inter-event spacing, deviations from Poisson statistics occur.

II.1.2 Afterpulsing

Radiation-induced traps within the silicon lattice can capture charge carriers during an avalanche. These carriers may later be released after a characteristic delay, potentially retriggering an avalanche in the same pixel. This phenomenon, known as afterpulsing, introduces correlated noise following an initial event. The probability of afterpulsing depends on factors such as the trap density and the lifetime of intermediate states introduced by the traps.

II.1.3 Recovery Time

After an avalanche event, the quenching resistor and pixel capacitance determine how quickly the electric field within the microcell recovers. The recovery process follows an exponential behavior:

$$V(t) = V_{\text{bias}} \left(1 - e^{-t/\tau_{\text{rec}}}\right), \tag{5}$$

where $\tau_{\text{rec}} = R_q C_{\text{cell}}$ is the recovery time constant, defined by the quenching resistor R_q and the pixel capacitance C_{cell}. A longer recovery time reduces the effective detection efficiency for subsequent photons but also decreases the probability of correlated avalanches.

II.1.4 Neutron Flux in the HL-LHC Environment

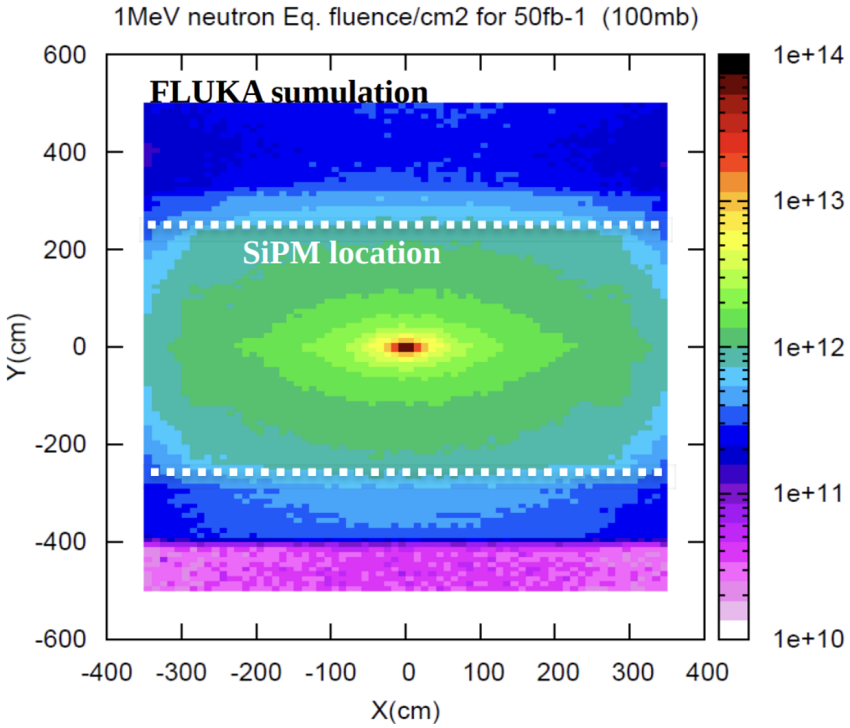

Figure 22: Simulated neutron flux distribution on the X–Y plane for the LHCb detector at the end of the HL-LHC operation [2].

In the SciFi detector system, the SiPM arrays are coupled to the scintillating fibres and positioned away from the beam centre. Consequently, they are exposed to a reduced neutron flux compared to on-axis detector components. Nevertheless, over the full High-Luminosity LHC (HL-LHC) operation cycle, the accumulated fluence is expected to reach approximately 3×10^{12} $\text{n}_{\text{eq}}/\text{cm}^2$. Such radiation exposure significantly alters the SiPM characteristics, leading to increased dark count rates and reduced reliability.

To mitigate these effects, the SiPMs will be operated inside a cryogenic cooling system at approximately 100 K. Lowering the temperature reduces the thermal generation rate of carriers, thereby suppressing the DCR exponentially according to Eqn. 3.

In this study, we aim to evaluate the expected DCR for SiPMs subjected to a fluence of 1×10^{13} $\text{n}_{\text{eq}}/\text{cm}^2$ at various overvoltages and temperatures around 100 K. The objective

is to identify and quantify the dominant contributions to dark signals under these extreme conditions, in preparation for the LHCb Upgrade II program.

II.2 Methodology

The SiPM under test was placed inside a cryostat equipped with a vacuum pump to remove the air and minimise convective heat transfer. Once a sufficient vacuum level was achieved, the cryostat was cooled to the target temperature using a cryogenic cooling system.

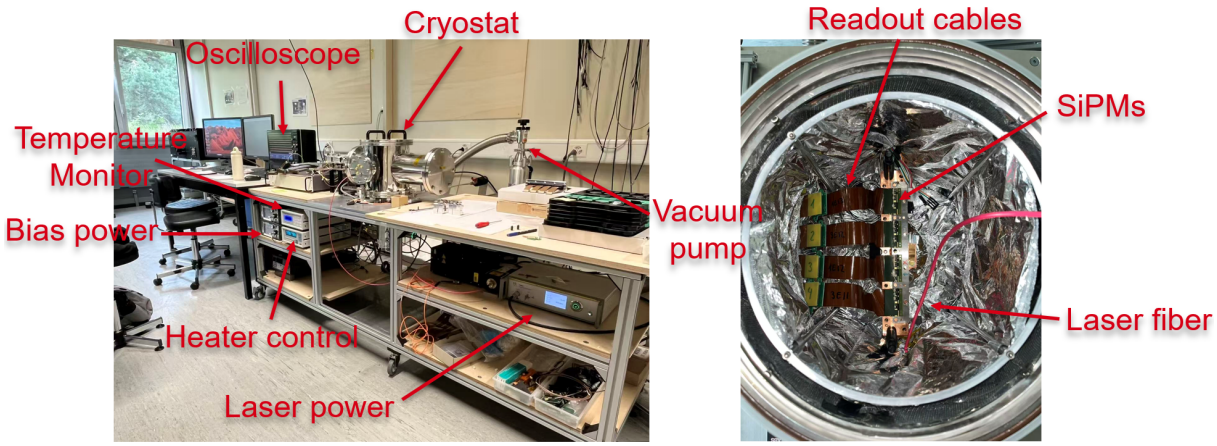

Figure 23: Experimental setup for DCR measurement.

To eliminate the effect of crosstalk, single-pixel SiPMs were used for all measurements. Two SiPM designs with different cell sizes, 31 µm and 42 µm, were investigated, as shown in Fig. 24.

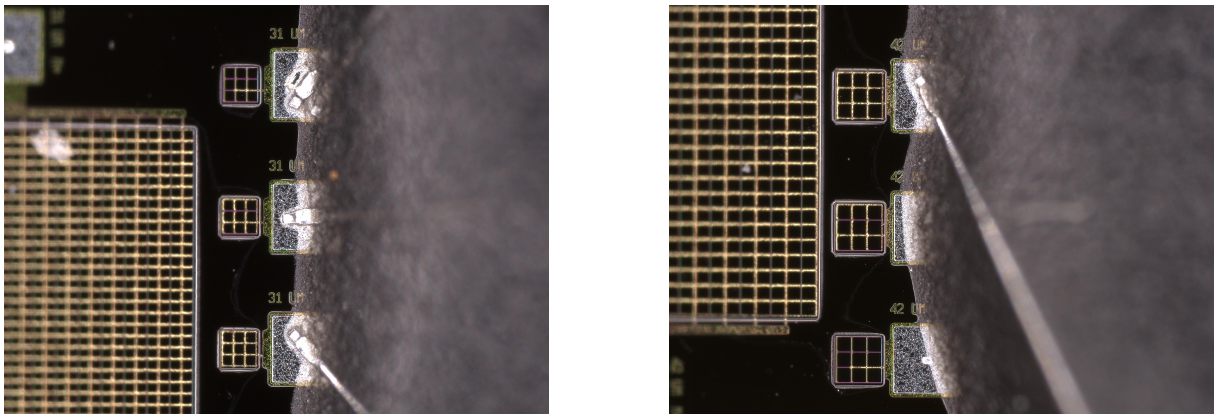

Figure 24: Single-pixel SiPMs used in the study. Left: 31 µm cells; Right: 42 µm cells.

II.2.1 Breakdown Voltage Determination

The breakdown voltage, V_{bd}, was determined using the Inverse Logarithmic Derivative (ILD) method [7]. In this method, the current of an individual SiPM channel is measured as a function of the applied bias voltage under controlled laser illumination.

The ILD is defined as

$$\mathrm{ILD}(I(V)) = \left(\frac{d}{dV}\ln I\right)^{-1} = I\frac{dV}{dI}. \tag{6}$$

In the voltage region just above the breakdown voltage, and assuming negligible crosstalk contribution, the SiPM current can be approximated by a power-law dependence on the overvoltage $\Delta V = V - V_{\mathrm{bd}}$:

$$I(V) \propto (V - V_{\mathrm{bd}})^{1+\kappa}, \tag{7}$$

where κ is a constant describing the voltage dependence of the photon detection efficiency (PDE).

Applying the ILD to this relationship yields a linear dependence:

$$\mathrm{ILD}(I(V)) = \frac{1}{1+\kappa}(V - V_{\mathrm{bd}}). \tag{8}$$

Thus, the ILD varies linearly with the applied voltage and becomes zero at $V = V_{\mathrm{br}}$. This property allows for a precise determination of the breakdown voltage by extrapolating the linear region of the ILD curve to the voltage axis. The method enhances accuracy by identifying the inflection point of the logarithmic current curve, corresponding to the onset of avalanche multiplication.

II.2.2 Dark Count Measurement Procedure

The DCR was then measured using an oscilloscope to record the SiPM output signals. In principle, the DCR should be determined under dark conditions (i.e., without illumination). However, at low overvoltages, both the pulse amplitude and the rate of dark counts become too small to distinguish from electronic noise. Under such conditions, weak laser illumination was introduced to generate a constant rate of optical triggers.

A 40 ms acquisition window was used for each measurement. All recorded waveforms were processed to extract the amplitudes of individual peaks and their time separation relative to the previous pulse. The results were visualised as a two-dimensional histogram, as shown in Fig. 25.

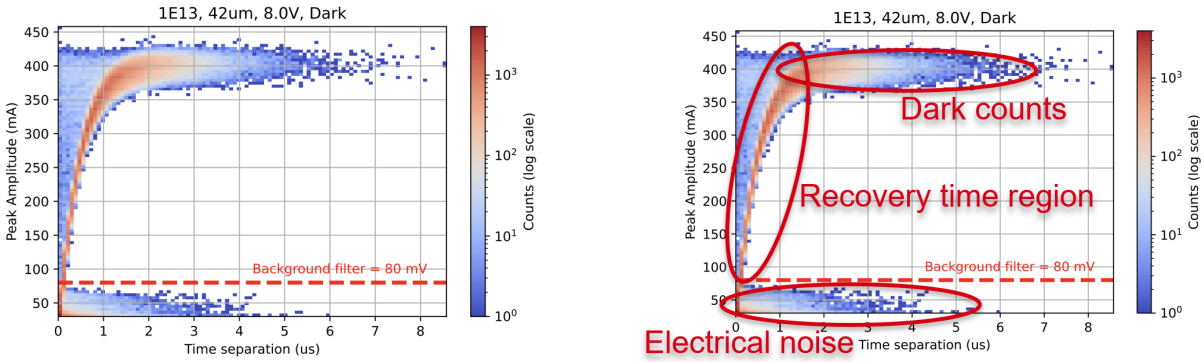

Figure 25: Left: Two-dimensional histogram of peak amplitudes versus their separation time. Right: Same plot with labelled regions corresponding to electrical noise, recovery-time effects, and dark counts.

A filtering threshold was applied to remove electronic noise. Projecting the histogram onto the amplitude axis yields the distribution shown in Fig. 26. The green region highlights the signal peaks selected for subsequent analysis of time separation.

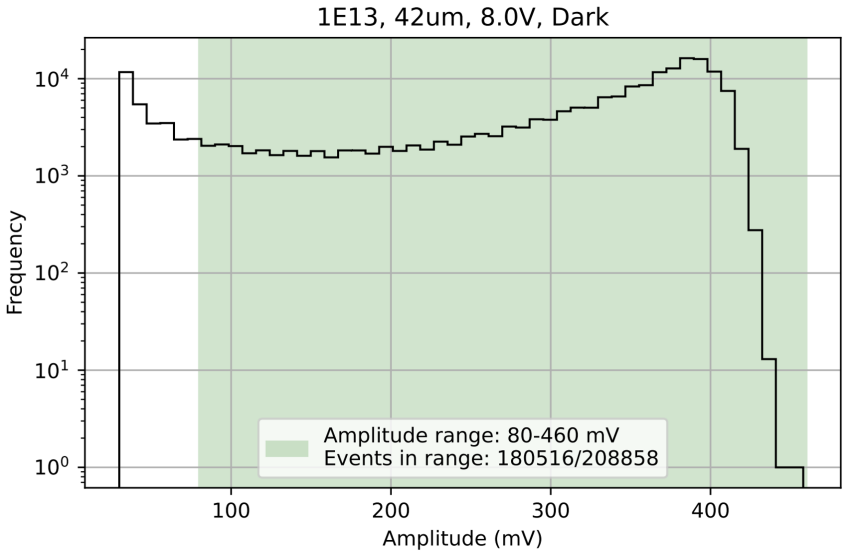

Figure 26: Amplitude distribution of all detected peaks. The green region indicates the selected range for time separation analysis.

The DCR was extracted by fitting a Poisson distribution to the time-separation histogram, as illustrated in Fig. 27.

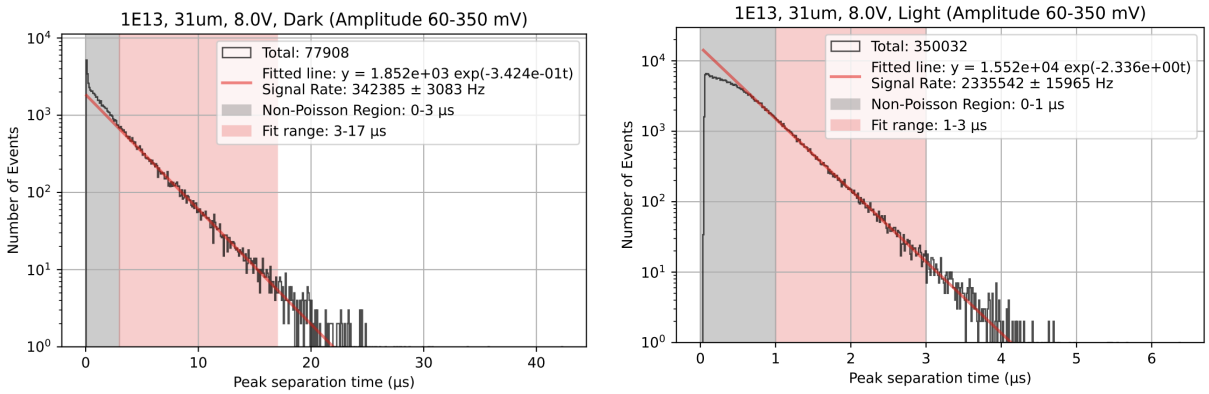

Figure 27: Left: Poisson fitting for a 31 µm SiPM at 8.0 V overvoltage under dark conditions, showing an excess at short time intervals due to afterpulses. Right: Same SiPM under illumination, exhibiting a deficit at short intervals attributed to recovery-time effects.

The excess at short time intervals is attributed to afterpulsing, whereas the deficit corresponds to the pixel recovery effect. Interestingly, for the 42 µm SiPM, this trend reverses as the overvoltage (and consequently the DCR) increases, as shown in Fig. 28.

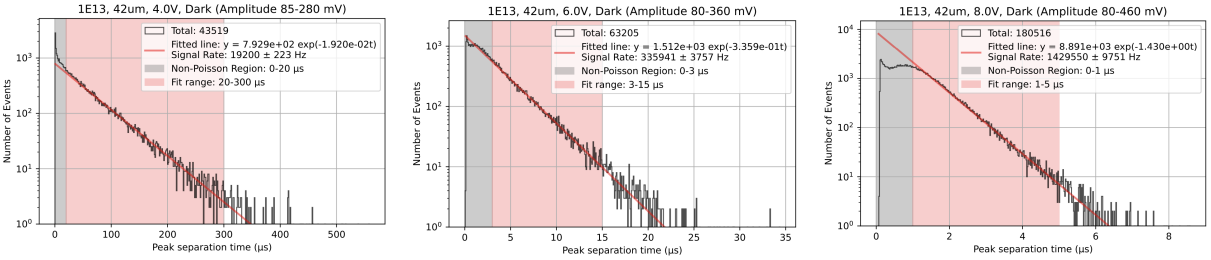

Figure 28: Poisson distribution fitting for the 42 µm SiPM under dark conditions at different overvoltages. Left: 4.0 V; Middle: 6.0 V; Right: 8.0 V. The deviation from Poisson statistics evolves from an excess to a deficit as the DCR increases.

II.3 Results

The signal rate for both the 31 µm and 42 µm SiPMs was extracted from the Poisson fitting results under both illuminated and dark conditions. The results are shown in Fig. 29.

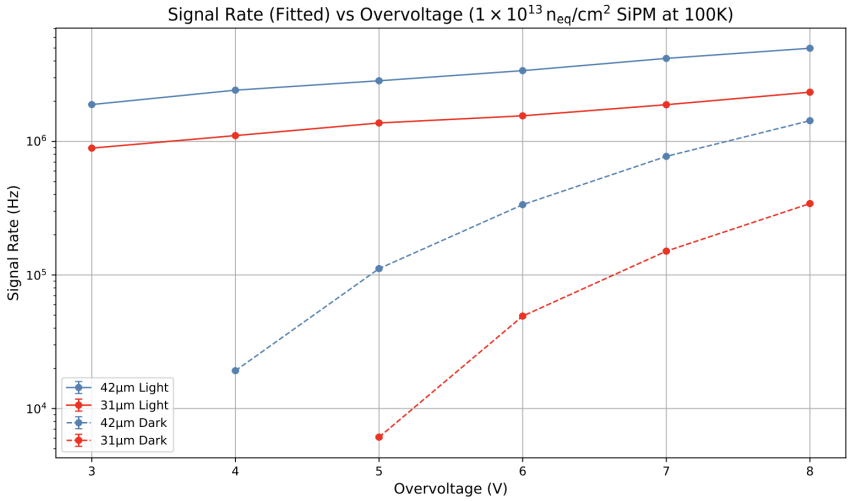

Figure 29: Signal Rate as a function of overvoltage for 31 µm and 42 µm SiPMs under illuminated and dark conditions. As expected, the signal rate increases with overvoltage, and the 42 µm device exhibits a higher signal rate due to its larger active volume.

Overall, the 42 µm cells exhibit higher DCR values, which is consistent with expectations since larger pixel areas provide a greater volume for thermally generated carriers to trigger avalanches. Similarly, illuminated SiPMs show a higher overall signal rate due to the additional photon-induced avalanches. In all cases, the rate increases monotonically with overvoltage.

When plotted on a linear scale, as shown in Fig. 30, a roughly constant offset is observed between the illuminated and dark datasets. This suggests that the difference is primarily due to the constant photon flux from the laser source.

This approximately constant difference between the illuminated and dark conditions aligns with the expectation of a uniform photon rate from the laser. However, further investigation is needed to determine whether this offset can be used to accurately extrapolate the DCR at low overvoltages, where the dark count rate becomes too small to measure directly. A naive extrapolation assuming a constant offset would yield unphysical negative DCR values at very low bias, indicating that the underlying dependence is more complex.

Additionally, the ratio between the measured and expected number of signals from the fitted Poisson distribution was evaluated, as shown in Fig. 31. This ratio provides a direct visualisation of deviations from Poisson statistics, indicating the presence of correlated noise processes such as afterpulsing or recovery-time suppression.

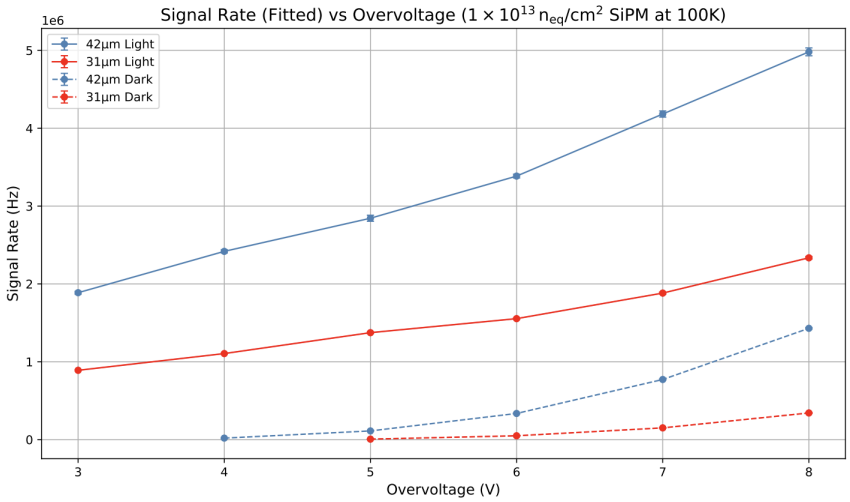

Figure 30: Signal Rate versus overvoltage (linear scale). A nearly constant offset between illuminated and dark measurements is observed, corresponding to the contribution from laser-induced events.

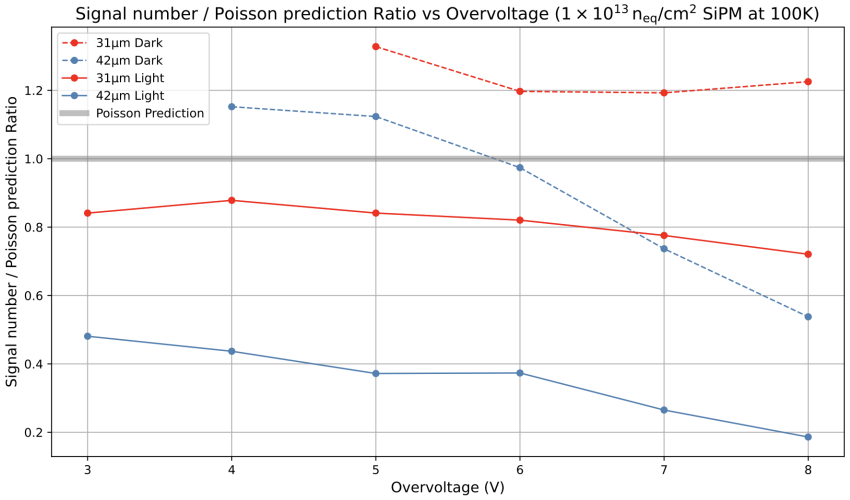

Figure 31: Ratio between the measured number of signals and the expected number from Poisson fitting. Values greater than 1.0 indicate an excess of events (afterpulsing), while values below 1.0 indicate a deficit (recovery-time suppression).

From this plot, illuminated cells consistently exhibit a deficit (ratio < 1), likely due to the high signal rate driving microcells into partial recovery. The 31 µm SiPM under dark conditions also shows a deficit, while the 42 µm device transitions from excess to deficit around 6 V overvoltage, consistent with the trend observed in Fig. 28.

II.4 Discussion

The overall results are in good agreement with previous studies. The expected dependence of DCR on pixel size and overvoltage is clearly observed. Furthermore, the transition between excess and deficit regions relative to the Poisson prediction provides qualitative evidence of the interplay between afterpulsing and recovery time effects.

The approximately constant offset between illuminated and dark conditions suggests the possibility of using illuminated data to estimate the DCR at low overvoltages where direct measurement becomes difficult. Although this analysis was not performed here due to time constraints, it represents a potentially useful method for future work.

The observed transition in deviation behaviour that shifts the number of signals from excess (afterpulsing-dominated) to deficit (recovery-limited) when compared to the Poisson distribution can be interpreted as a competition between these two processes. At low DCR, afterpulsing dominates due to the higher probability of trap-assisted retriggering within available recovery time. At higher DCR or overvoltage, the recovery time becomes a limiting factor, leading to a deficit in detected counts as more avalanches occur during the recharge period of neighboring cells.

A qualitative expression for the DCR probability distribution, accounting for both effects, can be proposed as:

$$P(t) = \left(C_{\mathrm{DC}} e^{-R_{\mathrm{DC}} t} + C_{\mathrm{AP}} e^{-R_{\mathrm{AP}} t}\right)\left(1 - e^{-t/\tau_{\mathrm{rec}}}\right), \tag{9}$$

where R_{DC} and R_{AP} are the rates of dark counts and afterpulses respectively, C_{DC} and C_{AP} are scaling constants, and τ_{rec} is the recovery time constant of the SiPM.

It is worth noting that each of these parameters, particularly R_{DC}, R_{AP}, and τ_{rec}, can depends on temperature, overvoltage, and accumulated radiation fluence. For instance, SiPMs irradiated to a fluence of 10^{13} $\mathrm{n_{eq}/cm^2}$ and operated at 100 K have been observed to exhibit non-Poissonian DCR distributions, while unirradiated devices at room temperature follow a near-ideal Poisson behavior. A systematic study of SiPMs across different fluence levels and operating conditions would thus provide deeper insight into the underlying mechanisms affecting DCR statistics.

References

[1] Harriet Jarlett. *25 years of Large Hadron Collider experimental programme. CERN celebrates 25 years since the beginning of the LHC experimental programme.* Accessed: 06-11-25. CERN. Dec. 2017. URL: https://home.cern/news/news/cern/25-years-large-hadron-collider-experimental-programme.

[2] LHCb Collaboration. *LHCb Tracker Upgrade Technical Design Report.* Tech. rep. 2014. DOI: 10.17181/CERN.OOOE.9O9T. URL: https://cds.cern.ch/record/1647400.

[3] Thomas Kirn and LHCb Collaboration. "SciFi – A large scintillating fibre tracker for LHCb". In: *Nuclear Instruments and Methods in Physics Research Section A* 845 (2017), pp. 481–485. DOI: 10.1016/j.nima.2016.06.057. URL: https://www.sciencedirect.com/science/article/pii/S016890021630599X.

[4] S. Vinogradov. "The Silicon Photomultiplier (SiPM) Concept and Design Development". In: *APPEC News* (Mar. 2015). Available at: https://www.appec.org/news/the-silicon-photomultiplier-sipm-concept-and-design-development/.

[5] *Single-Photon Avalanche Diode (SPADs).* MeetOptics Academy. Available at: https://www.meetoptics.com/academy/single-photon-avalanche-diode.

[6] PicoQuant GmbH. *Light Sources – Operation Manual and Technical Data.* Version 1.x (Operation Manual and Technical Data for PicoQuant light sources). Available at https://www.picoquant.com/downloads. PicoQuant GmbH. Berlin, Germany, 2025. URL: https://www.picoquant.com/downloads.

[7] V. Chmill et al. "Study of the breakdown voltage of SiPMs". In: *Nuclear Instruments and Methods in Physics Research Section A: Accelerators, Spectrometers, Detectors and Associated Equipment* 845 (2017), pp. 56–59. DOI: 10.1016/j.nima.2016.04.047. URL: https://doi.org/10.1016/j.nima.2016.04.047.